Received: Added at production | Revised: Added at production | Accepted: Added at production

DOI: xxx/xxxx

ARTICLE TYPE

Real-time rotor effective wind speed estimation based on actuator disc theory: design and full-scale experimental validation

Alan W.H. Lio* | Fanzhong Meng | Gunner Chr. Larsen

Department of Wind and Energy Systems, Technical University of Denmark (DTU), DK-4000 Roskilde, Denmark

Correspondence
*Alan W.H. Lio. Email: wali@dtu.dk

Summary

The use of state estimation techniques offers a means of inferring rotor effective wind speed from standard measurements of wind turbines. Typical wind speed estimators rely upon a pre-computed quasi-steady aerodynamic mapping, which describes the relationship between pitch angle and tip-speed ratio and the power coefficient. In practice, the static mapping does not capture the influence of turbine structural dynamics and atmospheric turbulence, inevitably resulting in poor performance of the wind speed estimation. In addition, the turbine aerodynamic properties might not be easily accessible. Thus, this paper presents a rotor effective wind speed estimation method that obviates the requirement for prior knowledge of turbine power coefficients. Specifically, the proposed method exploits a simple actuator disc model, where the aerodynamic power and thrust coefficients can be characterised in terms of axial induction factors. Based on this insight and standard turbine measurements, real-time estimation of rotor effective wind speed and axial induction factors can then be achieved using a simplified turbine drive-train model and an extended Kalman filter. In addition, the actuator disc model can be updated easily over time by calibrating solely two correction factors. Thus, the proposed algorithm presents an alternative for estimating the rotor effective wind speed, which is valuable for numerous applications, for example, LiDAR-assisted control and coherence studies.

KEYWORDS:
rotor effective wind speed, state estimation, Kalman filtering, control

1 | INTRODUCTION

The knowledge of wind speed is particularly valuable for large modern wind turbines and is crucially important for many control applications, for example, LiDAR-assisted control and correlation studies[1,2,3,4], disturbance accommodating control[5,6] and calculation of power reserve in down-regulation[7,8]. Typically, a wind speed measurement is available from the anemometer located at the top of the nacelle. The uncertainties in these measurements arise from a number of sources, for example, the rotor and nacelle induced flow disturbances, tower shadow and wind shear variations. In addition, the wind field across a large rotor can not solely be described by a single point measurement. Thus, the concept of rotor effective wind speed emerged, where a fictitious wind speed is defined as a weighted sum or spatial average of the wind speeds across the rotor plane[9,10]. Notice that rotor effective wind speed in this context is sometimes known as free mean wind speed or ambient rotor plane spatially-averaged wind speed[11]. One possibility is that the rotor plane spatially-averaged wind speed could be directly measured by LiDARs and time-shifted accordingly[2]. However, LiDARs are still relatively expensive rendering their use confined to research investigations, which in turn motivated the development of state observer and estimation techniques to infer the rotor effective wind speed from standard turbine measurements.

The problem of rotor effective wind speed estimation has been widely studied over the past two decades. The simplest approach is the *power balance method*, where the wind speed is inferred based on its static relationship with the electrical power (e.g. Bhowmik and Spee (1998)[12]). The drawback of this approach is that the system dynamics and losses in the drive-train were not considered[10]. A study by Østergaard et al (2007)[10] showed that using a dynamic model can significantly improve the estimation performance. First, the approach was to estimate the aerodynamic torque based on three elements: a simplified drive-train model, a linear unknown input observer and standard turbine measurements. The wind speed was subsequently computed using the estimated aerodynamic torque via the Newton-Raphson method. This method is popular and adopted in many works (e.g. Ma et al. (1995)[13], Østergaard et al (2007)[10], Moustakis et al. (2019)[14]). Moreover, some studies obviated the iterative gradient descent methods by augmenting the wind speed as an additional system state and using more advanced estimation techniques such as the extended Kalman filter by Knudsen et al. (2011)[15], multiple model Kalman filter used by Lio et al. (2020)[16], and immersion and invariance used by Ortega et al. (2011) and Ortega et al. (2013)[17,18], which is recently revisited by Liu et al. (2022)[19]. Besides exploring advanced estimation methods, some studies considered additional dynamics into the estimator models such as tower structures (e.g. Knudsen et al. (2011)[15]), dynamic inflow (e.g. Henriksen et al. (2012) and Knudsen et al. (2013)[11,20]) and wind shears (e.g. Simley et al. (2016)[21]). Detailed surveys and comparisons of rotor effective wind speed estimation can be found in Soltani et al. (2013)[22].

One of the applications of rotor effective wind speed is for assessing the quality of LiDAR measurements. The quality of LiDAR measurements is typically quantified in terms of correlation or coherence between the LiDAR measurement and wind speeds measured at hub height or from a met mast. The rotor effective wind speed resulting from the estimator can be a good alternative for evaluating the LiDAR performance. In addition, LiDAR measurement coherence is crucial for LiDAR-assisted control[23]. To reconstruct the actual wind speed seen by the turbine, an adaptive filter is often designed to filter the preview LiDAR signal based on the coherence[24,25].

Typical wind speed estimation methods rely on the quasi-steady aerodynamic characteristics of the turbine rotor, specifically the power coefficient. The aerodynamic characteristic is often pre-computed assuming an uniform wind inflow field in a steady state. In reality, this aerodynamic coefficient varies significantly upon the turbine operating and atmospheric conditions. For example, the flexibility of the rotor blade and/or the blade airfoil properties change over time due to erosion. Besides the technical perspective, turbine aerodynamic characteristics might be confidential and therefore not easily accessible by third parties rather than the turbine manufacturers. For example, LiDAR manufacturers or controller retrofit companies might not have direct access to the turbine blade properties, but they can obtain the turbine SCADA (supervisory control and data acquisition) measurements. Thus, estimating the rotor effective wind speed using the power balance method or based on an aerodynamic mapping, namely the power coefficient, is infeasible.

Instead of using the pre-computed tabulated coefficients, a study by Ødgaard et al. (2008)[26] demonstrated the possibility of real-time *estimation* of the power coefficient and wind speed. In this study, the dynamics of power coefficient and wind speed were decoupled based on their time scale. The power coefficient was modelled as a slowly varying state, whereas the wind speed was considered to fluctuate relatively faster. However, the fact is that the instantaneous power coefficient might change as fast as the wind speed, especially in the above-rated wind conditions, which makes separating the power coefficient and the wind speed difficult for the estimator. A recent study by Lio et al. (2021)[27] proposed a data-driven and learning-based approach to an estimator design. The power coefficient was reconstructed using Gaussian process regression based on a small set of time-averaged turbine measurements. Subsequently, the rotor effective wind speed was inferred using an extended Kalman filter and the reconstructed aerodynamic mapping.

This work proposes a rotor effective wind speed estimation method that obviates the prior knowledge of turbine aerodynamic characteristics. In particular, the proposed scheme exploits a simple actuator disc model, where the aerodynamic power and thrust coefficients can be characterised in terms of the axial induction factor. Subsequently, the proposed method is developed based on an extended Kalman filter. The rotor effective wind speed and the axial induction factor can then be inferred from the proposed algorithm using standard turbine measurements such as rotor speed, generator torque and tower-bottom fore-aft moment. Moreover, the actuator disc model can be easily updated over time by calibrating solely two correction factors, which is significantly simpler than reconstructing a power coefficient mapping using the machine learning method as in[27]. The proposed method is then validated using full-scale measurements from a Vestas V52 turbine at the DTU Risø campus. From an industrial perspective, the proposed estimator enables LiDAR coherence studies and optimisation without prior knowledge of the turbine aerodynamic properties. In addition, real-time power and thrust coefficient, derived from the estimated induction factors, can be used for some wind farm control strategies such as the minimum thrust coefficient down-regulation control[28,29] or closed-loop dynamic induction control[30].

The remainder of the paper is structured as follows. In Section 2, background information regarding the applied actuator disc model is presented. Section 3 presents a control-oriented model that contains the dynamics of drive-train, tower and inflow. In addition, the link between aerodynamic power and thrust coefficient is discussed. Section 4 presents the design of the proposed rotor effective wind speed estimator based on extended Kalman filtering and tuning of the estimator is subsequently discussed. In Section 5, discussions of the experimental set-up are presented, and in Section 6 the proposed method is validated using full-scale turbine measurements. Finally, section 7 outlines conclusions and future works.

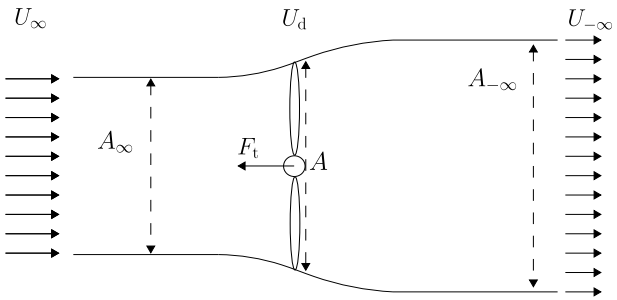

FIGURE 1 One dimensional actuator disc momentum theory.

2 | ACTUATOR DISC MODEL

The actuator disc model (ADM) is a well-known theory in the wind energy community [31] and is developed based on the momentum theory. The model considers the turbine rotor as a permeable disc that extracts kinetic energy from the incompressible wind flow, as shown in Figure 1. The wind speed upstream U_∞ is larger than the wind speed downstream $U_{-\infty}$, since the actuator disc is extracting kinetic energy from the wind. In addition, the cross-sectional area of the upstream stream-tube A_∞ must be smaller than the disc area A and the down-stream cross-sectional area $A_{-\infty}$, due to the conversation of the mass flow rate $\dot{m} := \frac{dm}{dt}$, defined as follows:

$$\dot{m} = \rho A_\infty U_\infty = \rho A U_\mathrm{d} = \rho A_{-\infty} U_{-\infty}, \tag{1}$$

where ρ denotes the air density, and U_d is the wind speed at the disc. Based on the balance of momentum upstream and downstream, a thrust force F_t and kinetic power (energy flux) P are developed at the uniformly loaded actuator disc, defined as follows:

$$F_\mathrm{t} = \dot{m}(U_\infty - U_{-\infty}), \;\; P = \frac{1}{2}\dot{m}(U_\infty^2 - U_{-\infty}^2) \tag{2}$$

It is convenient to express the thrust and power in terms of the undisturbed uniform upstream wind speed U_∞. The wind speed at the disc U_d is induced by the thrust acting upon the upstream free wind field and can be written as follows:

$$U_\mathrm{d} = U_\infty(1-a), \tag{3}$$

where a is the axial induction factor. Rearranging (2) yields the relation expressed in (4):

$$P = \frac{1}{2}(U_\infty + U_{-\infty})F_\mathrm{t} = U_\mathrm{d} F_\mathrm{t}. \tag{4}$$

Next, by substituting (3) into (4), the downstream wind speed can be written as follows:

$$U_{-\infty} = U_\infty(1-2a) \tag{5}$$

Therefore, the force acting on the flow F_t and the power extracted from the wind by the actuator disc P are derived by substituting the mass flow rate (1), wind speed at disc (3) and downstream wind speed (5) into (2) and (4):

$$F_\mathrm{t} = \frac{1}{2}\rho A U_\infty^2 4a(1-a), \;\; P = \frac{1}{2}\rho A U_\infty^3 4a(1-a)^2. \tag{6}$$

Finally, the thrust and power coefficients, in terms of axial induction factor a, are defined as follows:

$$C_\mathrm{t} = 4a(1-a), \;\; C_\mathrm{p} = 4a(1-a)^2, \tag{7}$$

where these non-dimensional coefficients are the ratio of the thrust and power in (6) over the thrust and power available in the air in absence of the actuator disc.

3 | CONTROL-ORIENTED MODELLING

This section presents the turbine structural and simplified aerodynamic models used in the estimator design.

3.1 | Turbine structural modelling

Typically, model-based state estimation requires a simplified and low-order model of the nonlinear system. The simplified model needs to capture the key dynamics of the turbine. A nonlinear turbine structural model, which includes the dynamics of the rotor drive-train (8) and tower (9), is presented.

First, the equation of motion of the drive-train is defined as follows:

$$J\dot{\Omega}(t) = Q_{\mathrm{a}}(t) - Q_{\mathrm{e}}(t)/n_{\mathrm{eff}}, \tag{8a}$$

where $\Omega \in \mathbb{R}$ is the rotor speed, the moment of inertia of the drive-train including the rotor is denoted as $J \in \mathbb{R}$ whilst Q_{a} and Q_{e} are the aerodynamic torque and generator torque at the low-speed side, respectively. Notice, that a direct drive-train with a gearbox ratio of 1 is assumed for brevity. The generator efficiency is denoted as $n_{\mathrm{eff}} \in \mathbb{R}$. The aerodynamic torque in (8) is modelled as follows:

$$Q_{\mathrm{a}} = \frac{1}{2}\rho\pi R_{\mathrm{r}}^2 C_{\mathrm{p}} U_{\infty}^3 \Omega^{-1}, \tag{8b}$$

where $R_{\mathrm{r}}, \rho \in \mathbb{R}$ are respectively the rotor radius and air density, whilst U_{∞} is the ambient wind speed.

Next, the tower-bottom fore-aft moment M_{fa} is modelled as follows:

$$M_{\mathrm{fa}} = H_{\mathrm{t}} \frac{1}{2}\rho\pi R_{\mathrm{r}}^2 C_{\mathrm{t}} U_{\infty}^2, \tag{9}$$

where $H_{\mathrm{t}} \in \mathbb{R}$ denotes the turbine hub height.

In this study, the measurements for the estimator are (i) rotor speed, Ω, and (ii) tower-bottom fore-aft bending moment, M_{fa}.

3.2 | A link between aerodynamic power and thrust coefficient

The quasi-static power and thrust coefficients $C_{\mathrm{p}}, C_{\mathrm{t}}$ are typically pre-calculated and tabulated in a two-dimensional table, respectively. However, this work exploits the simple actuator disc model to characterise these aerodynamic coefficients.

In the actuator disc model, the power and thrust coefficients in (7) are derived based on 1-dimensional (1D) momentum theory, and there are modelling errors compared to the realistic values of these coefficients due to many reasons. For example, the 3D aerodynamic effects, blade tip and root losses, errors due to deformation of the turbine tower and blades or wake rotation etc. Thus, additional multipliers are employed to compensate for the modelling errors, and the thrust and power coefficient are then defined as follows:

$$C_{\mathrm{t}} = 4a(1-a)\delta_{\mathrm{t}}, \;\; C_{\mathrm{p}} = 4a(1-a)^2\delta_{\mathrm{p}}, \tag{10}$$

where $\delta_{\mathrm{t}}, \delta_{\mathrm{p}} \in \mathbb{R}$ denote the correction factors in the thrust and power coefficients, respectively. The derivations of these correction factors will be discussed in Section 5.3.

3.3 | Dynamics of axial induction factor and wind speed

The axial induction factor a and ambient wind speed U_{∞} are unknown variables, which are considered as system states in the estimator. Their dynamics are modelled as random walk processes and driven by white noise, defined as follows:

$$a_{k+1} = a_k + n_a, \;\; n_a \sim \mathcal{N}\left(0, \sigma_a^2\right), \tag{11a}$$

$$U_{\infty,k+1} = U_{\infty,k} + n_U, \;\; n_U \sim \mathcal{N}\left(0, \sigma_U^2\right), \tag{11b}$$

where the subscript $k \in \mathbb{Z}^*$ denotes the sample time, and $n_a, n_U \in \mathbb{R}$ are the white Gaussian noises with zero mean and standard deviation $\sigma_a, \sigma_U \in \mathbb{R}$, respectively. Random walk processes are particularly suitable for estimation of unknown time-varying bias on the system state (e.g. [32]). The dynamics of axial induction factor and wind speed are inter-dependent on the size of the corresponding variances σ_a and σ_U. Selection of these values is discussed in Section 5.4.

4 | ESTIMATOR DESIGN

4.1 | Estimator model

Figure 2 illustrates the design of the rotor effective wind speed estimator, which is developed based on a well-known Kalman filtering approach [33]. The estimator employs the dynamics of the drive-train (8), the tower fore-aft moment (9), the wind inflow and axial induction factors (11). The

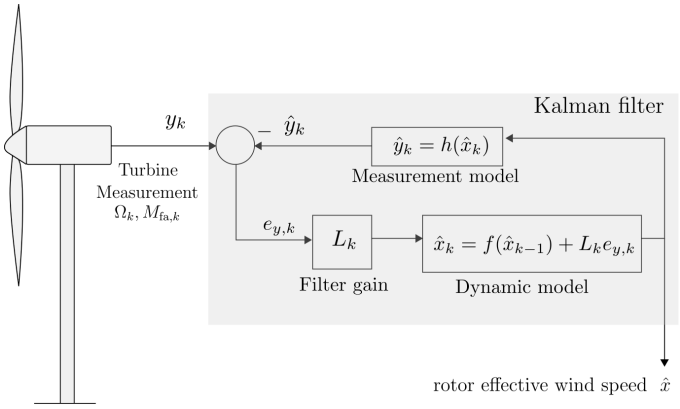

FIGURE 2 Design of the rotor effective wind speed estimator.

discrete-time representation of these nonlinear dynamics is described as follows:

$$x_{k+1} = f(x_k, u_k) + w_{\mathrm{n},k}, \tag{12a}$$

$$y_k = h(x_k) + v_{\mathrm{n},k}, \tag{12b}$$

where $x_k = [\Omega_k, a_k, U_{\infty,k}]^T \in \mathbb{R}^{n_x}$ denotes the system state vector, whilst $u_k = Q_{\mathrm{e,k}} \in \mathbb{R}^{n_u}, y_k = [\Omega_k, M_{\mathrm{fa,k}}]^T \in \mathbb{R}^{n_y}$ are the system input and output vectors. The state transition and output functions are denoted as $f : \mathbb{R}^{n_x} \times \mathbb{R}^{n_u} \to \mathbb{R}^{n_x}$ and $h : \mathbb{R}^{n_x} \to \mathbb{R}^{n_y}$, respectively. The process and measurement noises, $w_{\mathrm{n},k} \in \mathbb{R}^{n_x}$ and $v_{\mathrm{n},k} \in \mathbb{R}^{n_y}$, are assumed to be zero-mean stochastic variables with Gaussian distribution and are linearly added to the system. A detailed representation of (12) is as follows:

$$\underbrace{\begin{bmatrix} \Omega_{k+1} \\ a_{k+1} \\ U_{\infty,k+1} \end{bmatrix}}_{x_{k+1}} = \underbrace{\begin{bmatrix} \Omega_k + \frac{1}{J}\frac{1}{2}\rho\pi R_{\mathrm{r}}^2 4 a_k (1-a_k)^2 \delta_{\mathrm{p}} U_{\infty,k}^3 \Omega_k^{-1} \Delta t \\ a_k \\ U_{\infty,k} \end{bmatrix}}_{f(x_k,u_k)} + \underbrace{\begin{bmatrix} n_{\Omega,k} \\ n_{a,k} \\ n_{U,k} \end{bmatrix}}_{w_{\mathrm{n},k}} \tag{13a}$$

$$\underbrace{\begin{bmatrix} \Omega_k \\ M_{\mathrm{fa},k} \end{bmatrix}}_{y_k} = \underbrace{\begin{bmatrix} \Omega_k \\ H_{\mathrm{t}} \frac{1}{2}\rho R_{\mathrm{r}}^2 4 a_k (1-a_k) \delta_{\mathrm{p}} U_{\infty,k}^2 \end{bmatrix}}_{h(x_k)} + \underbrace{\begin{bmatrix} v_{\Omega,k} \\ v_{\mathrm{M},k} \end{bmatrix}}_{v_{\mathrm{n},k}} \tag{13b}$$

where $n_\Omega \in \mathbb{R}$ depicts the modelling error of the drive-train dynamics, while $v_\Omega, v_{\mathrm{M}} \in \mathbb{R}$ are measurements of the rotor speed and tower-base fore-aft bending moment, respectively. For numerical conditioning, the nonlinear model needs to be scaled properly, so that the measurement of the tower-base moment is of the same order of magnitude as the rotor speed measurement and other variables such as wind speed and axial induction factor.

4.2 | Extended Kalman filter

A Kalman filter is a computationally efficient and recursive algorithm that provides the optimal state estimates $\hat{x}_k \in \mathbb{R}^{n_x}$ of a *linear* system by minimising the mean squared state error, also known as the state error covariance matrix $P_k := \mathbb{E}\left((x_k - \hat{x}_k)(x_k - \hat{x}_k)^T\right)$. The filter is optimal for a stochastic dynamical system like (12) under a quadratic performance criterion and an assumption of white and Gaussian process and measurement noises. Since the filter model in this work is a *nonlinear* model (12), an extended Kalman filter (EKF) is employed to estimate the system states. The EKF is similar to the standard Kalman filter, except that it computes the estimates based on the nonlinear equations and determines the state covariance matrix P_k by linearising the system around the current state estimate.

The recursive filter alternates in two phases - prediction and correction - which are performed at every time step. In the prediction phase, the *a priori* system state (x_k^-), namely the state at current time k excluding the measurement at time k, is predicted based on the system model and the state estimate from the previous time step. In the correction phase, the predicted states are corrected by the system measurement at time k and the optimal Kalman filter gain, K, which minimises the error covariance. The corrected system state x_k^+ is known as *a posteriori* state. The statistical data of the estimated error, namely the covariance matrix P_k, is also updated in both phases as P_k^- and P_k^+, respectively.

A brief summary of the computational steps of the extended Kalman filter:

$$\text{(1) Intialise the filter :}$$

$$\hat{x}_0^+ = x_0,\ \ P_0^+ = Q,\ k = 0, \tag{14a}$$

$$\text{(2) Prediction :}$$

$$\hat{x}_k^- = f(\hat{x}_{k-1}^+, u_k),\ \ P_k^- = F_k P_{k-1}^+ F_k^T + Q, \tag{14b}$$

$$\text{where } F_k := \frac{\partial f(\hat{x}_{k-1}^+)}{\partial x}, \tag{14c}$$

$$\text{(3) Correction :}$$

$$\hat{y} = h(\hat{x}_k^-),\ \ \hat{x}_k^+ = \hat{x}_k^- + L_k(y_k - \hat{y}_k), \tag{14d}$$

$$P_k^+ = (I - L_k H_k)P_k^-,\ \text{ where } H_k := \frac{\partial h(x_k^-)}{\partial x}, \tag{14e}$$

$$\text{(4) } k = k+1,\ \text{Repeat step (2) and (3).}$$

where $L_k \in \mathbb{R}^{n_x \times n_y}$ is the filter gain, which is optimal when the performance criterion is to minimise the mean squared error $\mathbb{E}\left((x_k - \hat{x}_k^+)(x_k - \hat{x}_k^+)^T\right)$, and computed as follows[33]:

$$L_k = P_k^- H_k^T (H_k P_k^- H_k^T + R)^{-1}, \tag{14f}$$

where $Q \in \mathbb{R}^{n_x \times n_x},\ R \in \mathbb{R}^{n_u \times n_u}$ are the covariance matrices of the process and measurement noises, respectively.

4.3 | Estimator tuning and noise covariances

The tuning parameters of the proposed estimator are the process and measurement noise covariances Q and R. Theoretically, if the process noise w_n and measurement noise v_n are known, then the optimal covariances are $Q = \mathbb{E}[w_{\mathrm{n},k} w_{\mathrm{n},k}^T],\ R = \mathbb{E}[v_{\mathrm{n},k} v_{\mathrm{n},k}^T]^T$ under the assumptions that the noises are white and no mismatch between the model and real system[34]. Nonetheless, these noise statistics are typically unavailable, and therefore these covariances are often treated as tuning parameters for the estimator to achieve good performance. Typically, for reducing the problem complexity, these covariances are chosen to be diagonal matrices, similar to[35]. The covariance R is chosen based on the quality of the measurement sensor, defined as follows:

$$R := \mathrm{diag}\left(v_\Omega, v_M\right), \tag{15}$$

where v_Ω, v_M are the noise covariances of rotor speed and tower-bottom fore-aft moment measurements. Typically, these noise covariances are approximately 1-2% of the variance of the measurements[15]. The covariance Q describes the confidence of accuracy in the system modelling, defined as follows:

$$Q := \mathrm{diag}\left(w_\Omega, \sigma_a^2, \sigma_U^2\right), \tag{16}$$

where w_Ω is the degrees of model uncertainty in the drive-train, whilst σ_a and σ_U are the variances of the zero-mean white Gaussian noises in (11). Notice, that the effects of each tuning parameter are relative to others. The typical operating range of the axial induction factor is between 0 and 0.5[31]. Therefore, the parameter σ_a is chosen relatively smaller than σ_U, which equivalently makes the dynamics of the induction factor slower than that of the ambient wind speed. Filter tuning with full-scale data is discussed in Section 5.4.

5 | FULL-SCALE TURBINE EXPERIMENTAL SET-UP

5.1 | Full-scale turbine and LiDAR description

In the full-scale validation, the experimental turbine is the Vestas V52 at the DTU Risø campus. The turbine has a rotor diameter of 52 m, a hub height of 44 m and a rated power of 850 kW. The turbine was equipped with strain gauges on the tower, blade and shaft. Turbine measurements are collected at 4 Hz. Additional relevant turbine measurements are the rotor speed, generator torque at the low-speed side, generator power, tower-bottom fore-aft moment and hub-height wind speed.

The measurement campaign lasted approximately one year from June 2022 to July 2021. Figure 3 shows the V52 at the Risø campus with the spinner LiDAR at the top of the nacelle. The DTU spinner LiDAR is a continuous-wave Doppler Lidar that is mounted on the nacelle of the turbine. It was used to scan the upcoming wind inflow field at a rose pattern in front of the rotor[36]. The LiDAR probes a volume of air, providing

FIGURE 3 The V52 at the DTU Risø campus with SpinnerLiDAR installed on the nacelle. Photo by Erik Vogeley, DTU.

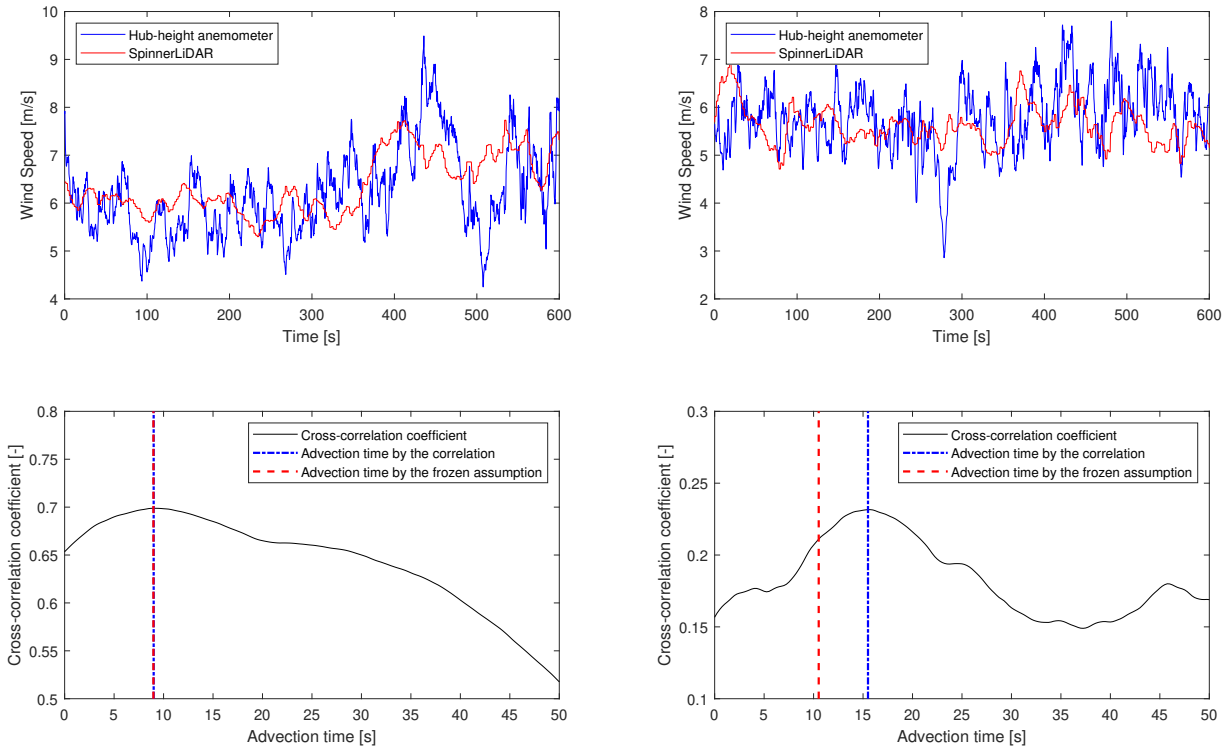

FIGURE 4 Time series (Top) and cross-correlation coefficient (bottom) between the hub-height anemometer and LiDAR measurements. The advection time is computed from the cross correlation where the correlation coefficient is at its maximum. Left: High correlation coefficient. Right: Low correlation coefficient.

a weighted volume average of the wind speed at the focal plane. The scanning rose pattern is completed every 2 seconds. Thus, the wind speed measurement is available at 0.5 Hz. Since the scans are recorded at low frequency, the LiDAR signal has much smaller fluctuations compared to the measurements obtained from the hub-height anemometer, which namely is a measurement at a single point and operating in the turbine wake. Therefore, the wind speed measured by the spinner LiDAR is more suitable to serve as the true rotor effective wind speed in this study.

5.2 | Advection time

The proposed estimator can infer the rotor effective wind speed at the rotor plane. To compare the estimated signal with the LiDAR measurement (ground truth), an advection time or time delay needs to be considered for the LiDAR signal. In typical LiDAR-assisted control (e.g. [25]), the advection time T_{d} is computed based on Taylor's frozen turbulence hypothesis, which assumes the turbulent wind structures move as frozen entities

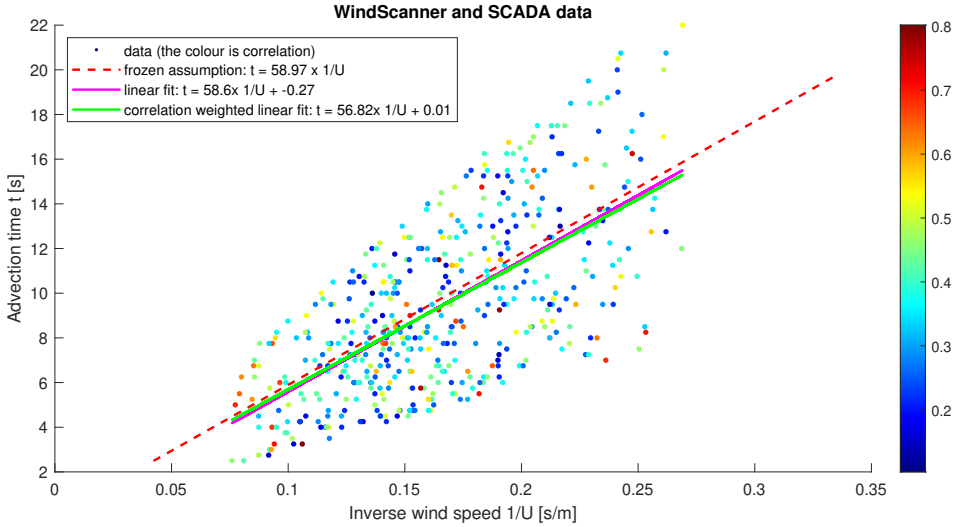

FIGURE 5 Comparison of advection times derived from Talyor's frozen turbulence assumption and correlation method, respectively.

transported by a characteristic mean wind speed:

$$T_{\mathrm{d}} = \frac{D}{\bar{U}} \tag{17}$$

where D denotes the distance between LiDAR measurement and the rotor plane, and $\bar{U}$ is the characteristic mean wind speed.

Alternatively, if the hub-height anemometer and LiDAR measurements are known, the advection time can be computed by finding the time lag that provides the maximum cross-correlation between these two signals[37,38]. The correlation coefficient of these two time series can also be calculated. Figure 4 shows examples of time series of the hub-height anemometer and spinner LiDAR. The variability in the huh-height measurement is expected to be much higher than the LiDAR signal, because the hub-height anemometer is subject to flow distortions from the nacelle as well as increased turbulence in the turbine wake. Moreover, it is considered a one point measurement, while LiDARs take a spatial average of the wind speed along the laser beam. The cross-correlations between the hub-height anemometer and LiDAR measurements are shown at the bottom of Figure 4. The left plot demonstrates a good alignment between the advection times calculated by the frozen turbulence method (red dashed line) and the correlation method (blue dashed line), which is confirmed by a high correlation coefficient of approximately 0.7. In contrast, a poor match of the advection time is shown in the right plot with a correlation coefficient of roughly 0.23.

From the full-scale experiment, the collected LiDAR signals and hub-height (SCADA) measurements are checked and the advection time is computed based on the correlation method. Some measurements that were of poor quality and provided insensible advection times were removed. Figure 5 shows the advection time estimated using the correlation method against the inverse of the mean wind speed of the LiDAR signal. The correlation coefficients are shown in colour. The advection time derived from the frozen turbulence hypothesis is shown in a red dashed line. A linear fit is computed based on the data (magenta line) and in addition, a weighted linear fit is also calculated based on the correlation coefficient (green line). A good agreement was found between the advection time by the frozen turbulence assumption and by the correlation method, respectively. Thus, for the purpose of the full-scale validation of the proposed wind speed estimator, the spinner LiDAR measurements would be time-shifted based on Taylor's frozen turbulence hypothesis. This set of good quality measurement data will be used for the full-scale validation in Section 6, representing the ground truth of the rotor effective wind speed.

5.3 | Discussions on model calibration

By observing (10), the correction factors, $\delta_{\mathrm{t}}, \delta_{\mathrm{p}}$, that influence the estimation of the induction factor, a and ambient wind speed, U_{∞}, can be evaluated. In absence of the model correction factors, the wind speed and induction factor estimates would be biased due to the simplistic character of the applied actuator model. Typically, a calibration problem also exists for the pre-computed power coefficient tables. However, calibration of the introduced two correction factors is much easier and less computationally demanding than updating the whole two- or three-dimensional table.

The correction factors can be calibrated by a collection of 10-minute time-averaged power and thrust coefficients, which can be computed using the turbine measurements. The 10-minute average power and thrust coefficients can be computed from available measurements as follows:

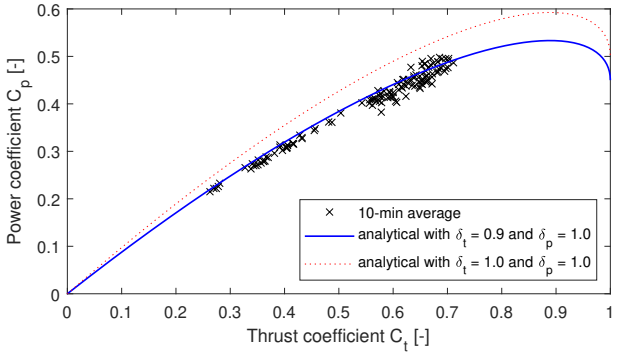

FIGURE 6 Power and thrust coefficients were computed based on full-scale turbine measurements of the Vestas V52 turbine. A comparison is made against the analytical model (10).

$$\bar{C}_{\mathrm{p}} = \frac{\bar{P}_{\mathrm{g}}/n_{\mathrm{eff}}}{\frac{1}{2}\rho A \bar{U}_{\mathrm{hub}}^3}, \quad \bar{C}_{\mathrm{t}} = \frac{\bar{M}_{\mathrm{fa}}/H_{\mathrm{t}}}{\frac{1}{2}\rho A \bar{U}_{\mathrm{hub}}^2}, \tag{18}$$

where $\bar{(.)}$ denotes 10-minute time-average, U_{hub} denotes hub-height wind speed measurement and P_{g} is the generator power.

Figure 6 illustrates the power and thrust coefficients calculated using (18) based on the measurement of the full-scale V52 turbine. The analytical expressions of C_{p} and C_{t} (10) are also shown in Figure 6, with the axial induction factor being less than $a \leq 0.5$ for usual operating condition of wind turbines[31]. By choosing the correction factor $\delta_{\mathrm{t}}, \delta_{\mathrm{p}}$ appropriately, the C_{p} and C_{t} from the analytical expressions (10) can match with the power and thrust coefficients from the measurements. In this particular case, these values are $\delta_{\mathrm{t}} = 0.90$ and $\delta_{\mathrm{p}} = 1$ for the full-scale V52 turbine.

5.4 | Discussions on Kalman filter tuning and consistency

The Kalman filter is appropriately tuned or statistically consistent if the estimation errors between the system states ($x_k - \hat{x}_k$) and the errors between the measurements ($e_k := y_k - h(\hat{x}_k)$) are (i) *Gaussian* and (ii) *white*[39]. In other words, the statistics of the state and measurement errors should be consistent with the chosen covariances Q and R. Since the truth system state x_k is often hard to obtain, filter tuning is typically done by examining the measurement errors e_k, which is also known as the innovation. By definition of a well-tuned filter, the innovation sequence e_k should have a zero mean and approximately 99.7% of the innovations should be bound within $\pm 3\sigma_j$, where $\sigma_j := H_{j,k} P^- H_{j,k}^T + R_{j,j}$ and $H_{j,k}$ is the jth row of H_k and $R_{j,j}$ is the jth diagonal element of R.

To tune the Kalman filter, this study used 1-day samples or 3,456,000 samples. The samples cover both below-rated and above-rated wind conditions as shown in Figure 7. Based on the samples, the proposed estimator is tuned to make the innovation sequences satisfy the Gaussian assumption. To simplify the tuning process, two innovation sequences in this study can be normalised into one quantity. That is the normalised innovation squared, denoted as $\nu_k := e_k^T S_k^{-1} e_k$. The normalised innovation squared is expected to be chi-squared distributed with n_y degrees of freedom ($\nu_k \sim \chi^2_{n_y}$)[a]. In other words, the normalised innovation squared ν_k must lie within the confidence interval $\nu_k \in [F_\chi^{-1}(\frac{1}{2}\alpha, n_y), F_\chi^{-1}(1 - \frac{1}{2}\alpha, n_y)]$, where F^{-1} is the inverse cumulative distribution function of the chi-squared distribution (in Matlab, *chi2inv*). In this case, the number of measurements is $n_y = 2$, thus the upper and lower bound are $[F_\chi^{-1}(0.025, 2), F_\chi^{-1}(0.975, 2)] = [0.05, 7.38]$ with $\alpha = 0.05$ (two-sided 95% confidence interval).

Figure 8 shows most of the normalised innovation squared lies within the confidence intervals, and the right plot shows the cumulative distribution of the normalised innovation squared ν. Thus, the hypothesis is acceptable and the innovation sequences e_k are unbiased Gaussian distributed, as shown in Figure 9. Notice that in Figure 9 during day time (10:00h-17:00h) the wind speed was above-rated, and the innovations were relatively larger. This might suggest that an adaptive tuning approach could be beneficial where the parameters Q and R could be adjusted depending on the wind speed, for example,[15].

Besides assessing the Gaussian property of the innovations, their whiteness needs to be tested. To examine if the innovation e_k is white, its sequence should be uncorrelated. Figure 10 shows the normalised autocorrelations of the innovation sequences. For rotor speed estimation error,

[a]For a well-tuned filter, the innovation sequence of each measurement is expected to be Gaussian distributed $e_j \sim \mathcal{N}(0, \sigma_j^2)$, that can be normalised as a sequence with a standard Gaussian distribution with unit variance $e_j/\sigma_j \sim \mathcal{N}(0, 1)$. The normalised innovation squared $v_k = e_k^T S_k^{-1} e_k$ is the sum of the square of j Gaussian distributed random variables with unit variance, thus, the normalised innovation squared is expected to be chi-squared distributed by definition $v \sim \chi_j^2$.

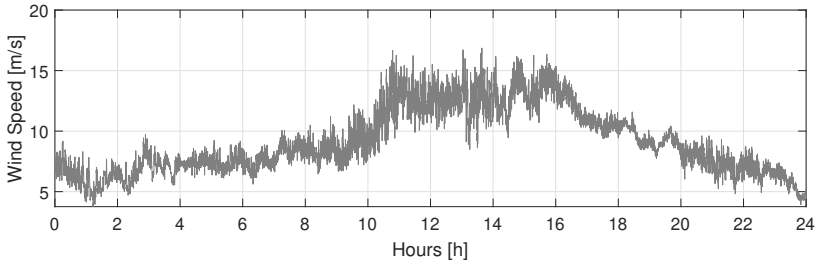

FIGURE 7 Wind speed of the samples used for filter tuning.

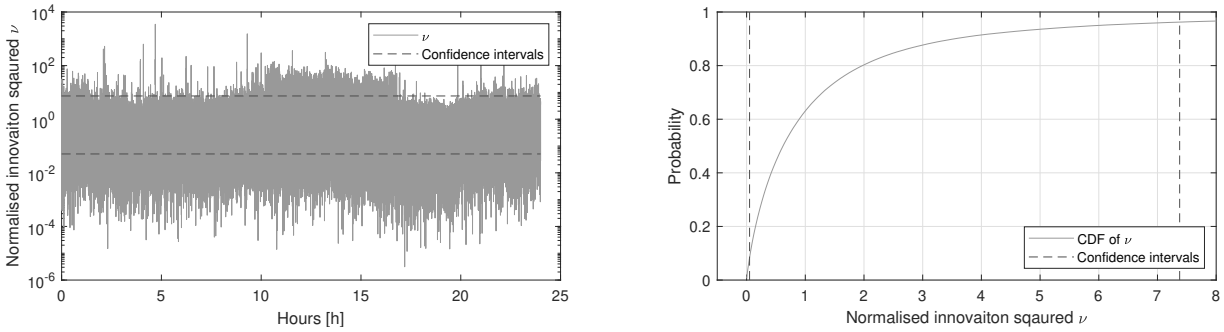

FIGURE 8 Left: Normalised innovation squared test, where 95% of the normalised innovation squared is bound by the confidence intervals defined by the χ^2 distribution. Right: Cumulative distribution function of the normalised innovation squared

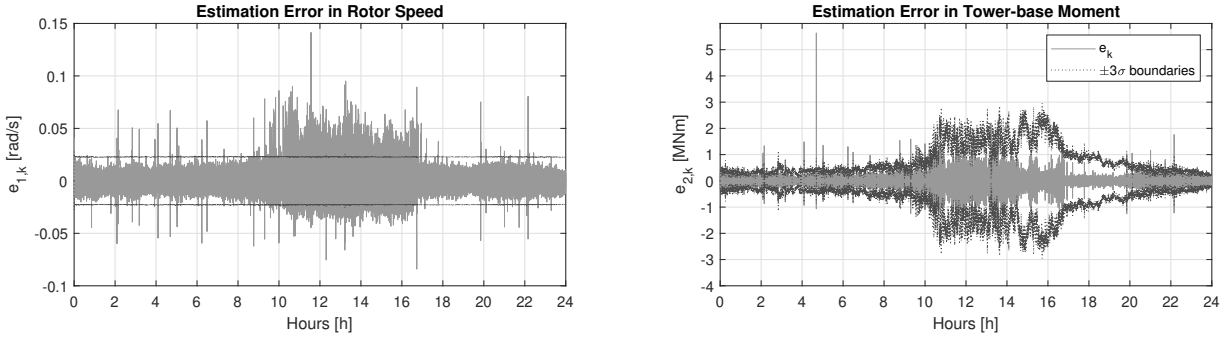

FIGURE 9 Innovations and their standard deviations $\sigma_k = \sqrt{S_k}$.

there was no clear sign of correlation. In contrast, the autocorrelation sequence of the tower-base moment error $(\mathrm{acf}(e_2))$ shows some correlations, which indicates some dynamics were not properly captured in our filter model. The harmonics appear at the multiple of 6 lags, which corresponds to the turbine tower natural frequency of 0.66 Hz. This correlation could be mitigated by modelling the tower as a second-order dynamics rather than a rigid body as in Equation (9). However, the trade-off is that the model complexity and tuning variables would increase, and additional knowledge of turbine structure would be required.

6 | FULL-SCALE VALIDATION

6.1 | Estimation performance in below-rated, around rated and above-rated wind conditions

This section demonstrates the efficiency of the proposed method on three 10-minute samples covering different wind conditions. Figure 11 demonstrates the time series of (i) the true rotor effective wind speed measured by the spinner LiDAR; (ii) the estimated wind speed using the proposed EKF based on an actuator disc model and (iii) the estimated wind speed by a standard EKF based on a power coefficient table generated

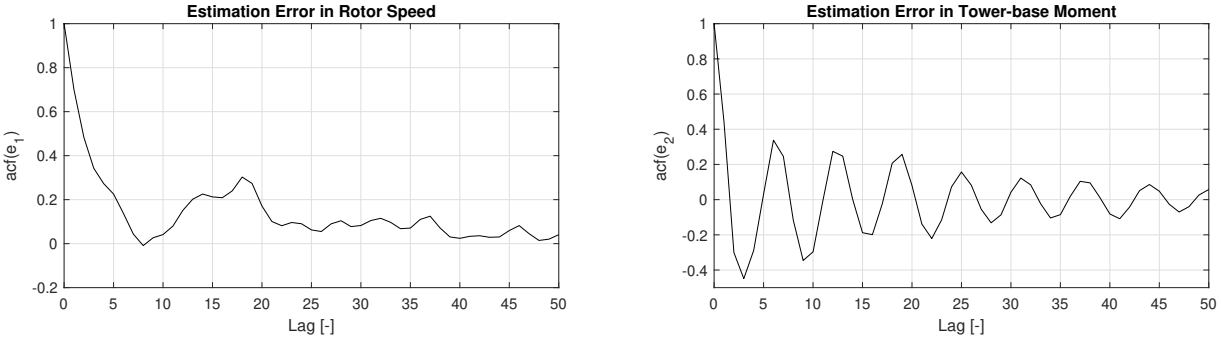

FIGURE 10 Normalised autocorrelation of the innovations.

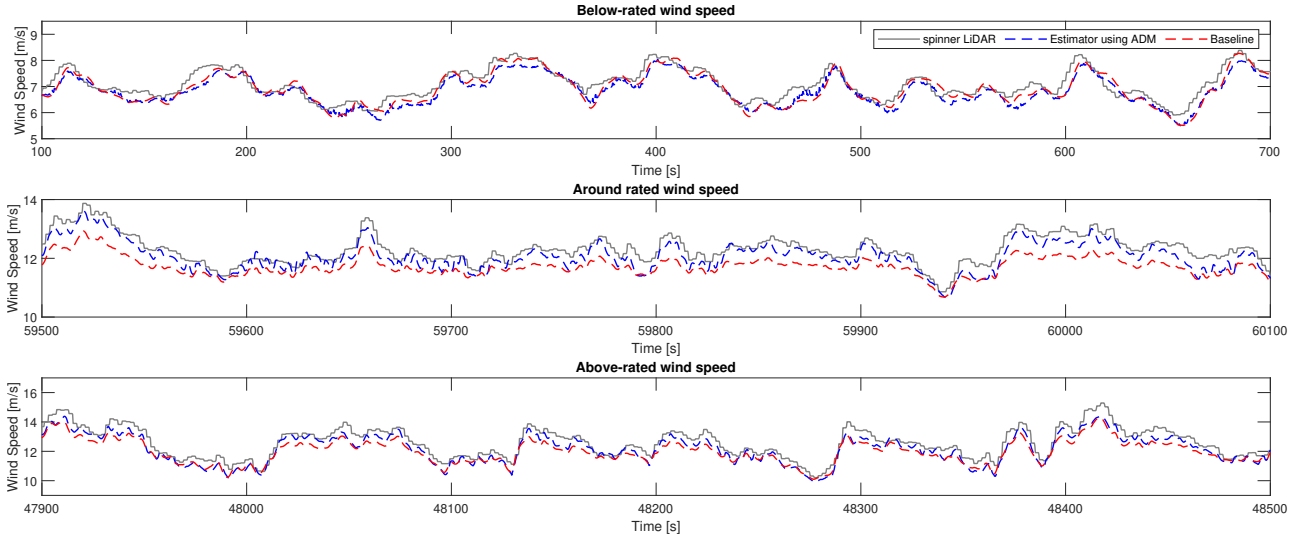

FIGURE 11 Time series of the wind speeds (i) measured by the spinner LiDAR, (ii) inferred by the proposed estimator using the actuator disc model and (iii) inferred by a traditional estimator using a pre-defined aerodynamic coefficient table (baseline). Three operating conditions were investigated: below-rated (top), around rated (middle) and above-rated (bottom) wind speed regions.

TABLE 1 Performance of wind speed estimator based on pre-defined table and actuator disc model.

	Below-rated ($\bar{U}$ = 7.08 m/s)		Around rated ($\bar{U}$ = 12.30 m/s)		Above-rated ($\bar{U}$ = 13.25 m/s)	
	Baseline	Estimator based on ADM	Baseline	Estimator based on ADM	Baseline	Estimator based on ADM
mean error [m/s]	-0.16	-0.24	-0.57	-0.24	-0.76	-0.47
std error [m/s]	0.24	0.22	0.20	0.16	0.29	0.26
RMSE [m/s]	0.29	0.33	0.60	0.29	0.81	0.54

by aero-elastic code HAWCStab2[40], which is the *baseline* in this study. Three operating conditions were investigated, namely below-rated (7.08 m/s), around rated (12.30 m/s) and above-rated (13.25 m/s) wind speed regions. The proposed method without using any knowledge of the rotor aerodynamic properties managed to achieve similar estimation performance in all cases compared to the baseline. Particularly, in the around and above-rated wind regions, the proposed estimator outperformed the traditional estimator with prior knowledge of the turbine power coefficient.

Figure 12 shows comparisons of relative errors of the wind estimates in three different wind conditions. The plots showed that the proposed estimator based on the ADM was able to achieve similar performance compared to the baseline method. In the around and above-rated conditions, the proposed method clearly outperformed the baseline. There could be a few explanations. (i) In the proposed estimator, the actuator disc model

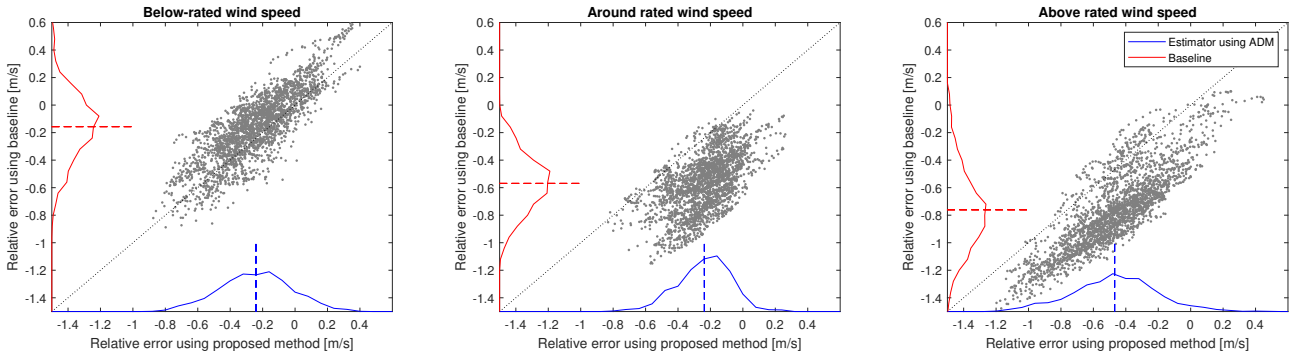

FIGURE 12 Comparisons of relative errors of the wind speed estimated by EKFs based on the actuator disc model (ADM) and traditional predefined aerodynamic table (baseline) in three different wind conditions. The dots shows samples of the 10-minute time series. The solid lines show their histograms and the dash lines denote means of the relative errors.

was calibrated using real measurement data, resulting in a better and more accurate filter model for the EKF; (ii) In the baseline estimator, the predefined aerodynamic table was derived from the aero-elastic tool, where the two-dimensional (2D) table was generated under steady wind speed. In addition, a 2D table is not sufficient to contain the power coefficient (C_p) for turbines with flexible blades, as there might exist more than one value of C_p for the same tip-speed ratio[27]. For example, for the same tip-speed ratio, there could exist a range of wind speed and rotor speed. Due to the blade deformation under different wind speeds, the C_p value would be different even though the tip-speed ratio is the same. Statistical results of the samples are summarised in 1.

6.2 | Robust performance to changes in atmospheric conditions

This section reveals how robust the proposed estimator is to the changes in atmospheric conditions, namely, the mean wind speed, the turbulence intensity and the wind shear. The performance of the proposed estimator is demonstrated on the selected measurement data set from Section 5.2. The baseline and proposed estimator were then applied to each time series to infer the wind speed estimates, and each time series consists of 700 seconds. Notice that the first 100-second estimate of each time series is discarded for initialisation reasons (i.e. system equilibrium is not yet achieved). The estimates were then compared with the time-shifted spinner LiDAR measurements based on the frozen wake hypothesis, which in turn yields the estimation errors.

Figure 13 shows the statistical mean and standard deviation of the estimation errors by both estimators. From each 10-minute time series, the mean error and standard deviation were obtained. Subsequently, for visualisation purposes, these data were then divided into bins based on mean wind speed, turbulence intensity and wind shear exponent. The left column of Figure 13 shows the mean estimation errors in different mean wind speeds, turbulence intensities (TIs) and wind shear exponents, whereas the standard deviations of the estimation error were shown in the right column.

The upper left plot of Figure 13 shows that most of the mean errors for both estimators were within ± 1 m/s for all mean wind speeds. As the mean wind speed increases, the performance difference between both estimators signifies, where the mean error of the baseline increases gradually in the above-rated wind regime (e.g. at 15 m/s). In contrast, the proposed estimator managed to keep the mean error around zero. These results confirm the earlier observations in the example cases in Section 6.1. The key reason was that the proposed method does not rely on any predetermined aerodynamic tables, which were often computed under simplifying assumptions (e.g. steady wind conditions) and furthermore have difficulties capturing the effect of blade deformations in a two-dimensional form. The upper right of Figure 13 shows the standard deviation of the error. It can be seen that most of the standard deviations were within 0.5 m/s and they were not changed significantly as the wind speed increased.

The middle row of Figure 13 shows the results of the mean and standard deviation of the errors against different inflow turbulence intensities. In both plots, there is a clear trend that the means and standard deviations would increase as the TI increased. The performance of both estimators was alike, where the mean errors of both estimators were within ± 1 m/s. This is because the model of wind *dynamics* in both estimators were identical and assumed to be a random walk process. These errors in terms of the means and standard deviations could be minimised, if an adaptive model for the wind speed was included that takes into account the turbulence intensity. See[15].

The bottom left plot of Figure 13 demonstrates the mean errors of both estimators generated under different wind shear conditions. Considering the normal range of the wind exponents between 0.1 and 0.4, the mean errors of both estimators increase gradually as the wind shear exponents grow. This is because, in both estimator models, the rotor imbalance caused by the wind shears was not considered (i.e. the applied actuator disc model assumes a uniform inflow field). In the ADM method, it is assumed that the thrust force is uniformly loaded across the rotor disc, while in

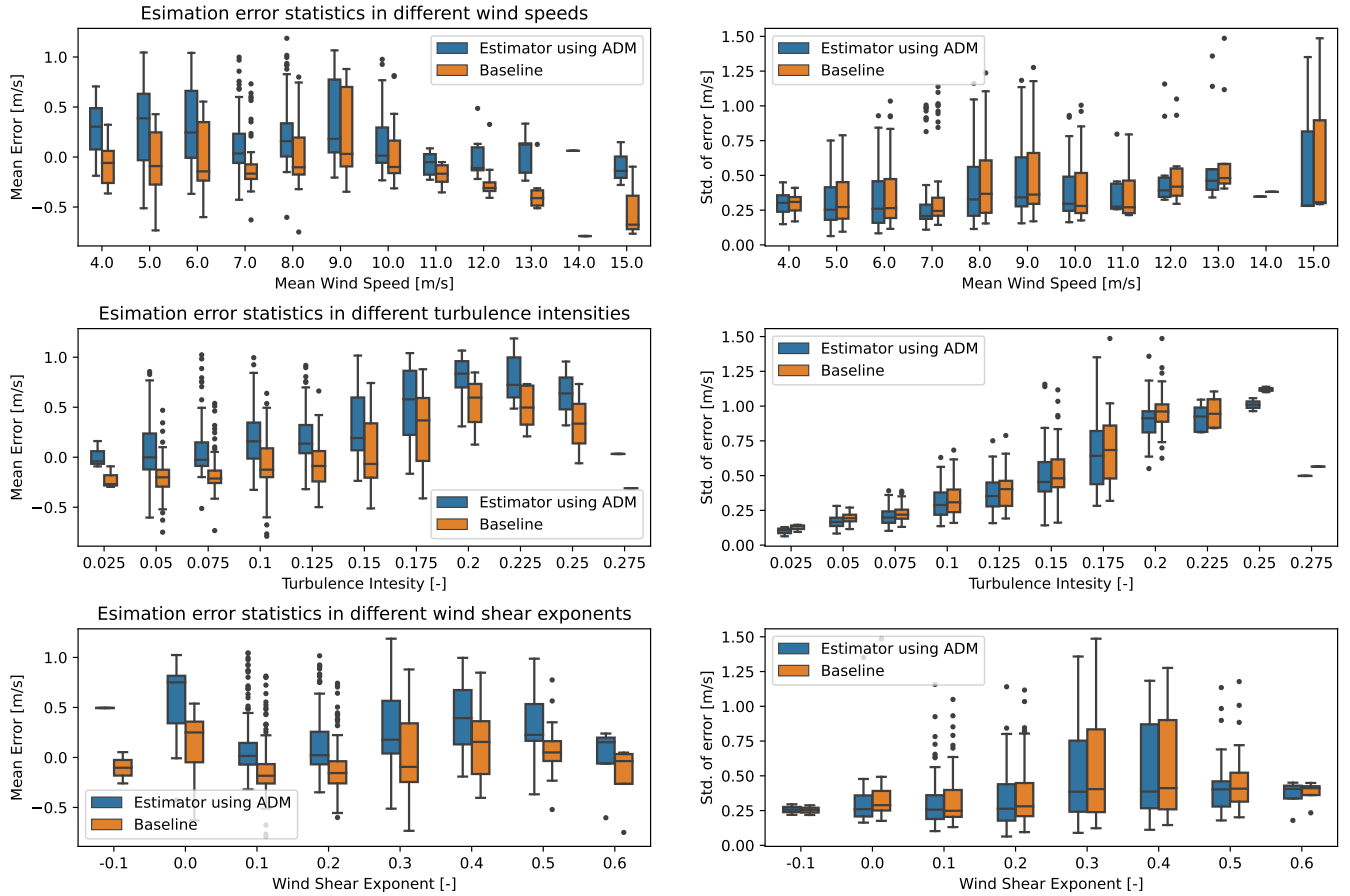

FIGURE 13 Statistical means (left) and standard deviations (right) of the estimation errors by the proposed estimator using ADM and the baseline estimator in different atmospheric conditions. The atmospheric conditions are grouped by mean wind speeds (top), turbulence intensities (middle) and wind shear exponents (bottom).

the baseline method, the power coefficient table is computed under a uniform wind flow. The bottom right plot of Figure 13 shows the standard deviations of the estimation error. At lower wind shear exponents, both estimators likely performed better in terms of providing lower standard deviations of the errors. The standard deviations of the errors spread wider or were more uncertain at some higher wind shear conditions, for example, 0.3 and 0.4. This is most likely due to the fact that the effect of the wind shear was not taken into account in the actuator disc modelling.

6.3 | Application: coherence study using the proposed wind speed estimator

The proposed method offers a means of estimating the rotor effective wind speed at the rotor plane without any prior knowledge of turbine blade aerodynamics. One of the practical applications is the LiDAR coherence study, where LiDAR manufacturers or controller retrofit companies might not have access to the blade properties.

The LiDAR coherence study was conducted based on the three 10-minute time series used in Section 6.1. A coherence study is typically employed to compare the correlation between LiDAR measurement and rotor effective wind speed. The study is crucial for LiDAR-assisted control, as it determines what range of frequency of the measured wind speed should be used for control. In addition, the study also can demonstrate the quality of the LiDAR signals. Figure 14 shows the magnitude-squared coherence between the spinner LiDAR and both estimated wind speeds. Both results were similar, for example, the frequency at which the coherence drops below 0.5 was 0.055 Hz for both methods. Therefore, the proposed method is a reliable wind speed estimation alternative for applications where the prior knowledge of turbine aerodynamics is unknown.

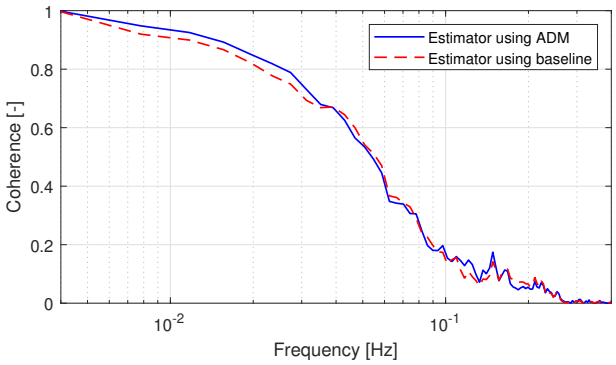

FIGURE 14 Magnitude-squared coherence between the spinner LiDAR measurements the and estimated wind speeds by (i) the proposed estimator using an actuator disc and (ii) a traditional estimator using a pre-defined aerodynamic coefficient table.

7 | CONCLUSIONS AND FUTURE WORKS

This paper presented a wind speed estimator design based on a simple actuator disc model. The simple actuator disc model characterised the power and thrust coefficients in terms of the axial induction factor. Based on this insight, the rotor effective wind speed and the axial induction factor could be inferred using standard turbine measurements, which were rotor speed, generator torque and tower-bottom fore-aft moment. The proposed design was validated on full-scale turbine measurement, demonstrating its reliable estimation performance, which was as good as the traditional method, where, however, no prior knowledge of turbine aerodynamics was needed by the innovative proposed method.

Despite the fact that the proposed wind speed estimator demonstrated a promising result, some further studies can still be done for improving the accuracy of the wind speed estimates. For example, the filter model for both methods (baseline and proposed) did not consider the changes in air density. Over the experimental period, the air density might be slightly different. In addition, the filter model can be updated to capture the changes in atmospheric conditions such as turbulence intensities or wind shear. For example, a study by [15] decoupled the mean wind speed and the turbulent wind speed fluctuations in the wind flow model. Also, a wind shear model (e.g. [21]) can be included in the wind speed estimator, which could potentially obviate the effect of wind shear on the wind speed estimates. This remains a topic for future work.

ACKNOWLEDGEMENT

This research was supported by the Energy Technology Development and Demonstration Program (EUDP), LiDAR assisted control for reliability improvement (LICOREIM, Grant No. 64019-0580).

References

1. Schlipf D, Cheng PW, Mann J. Model of the correlation between lidar systems and wind turbines for lidar-assisted control. *Journal of Atmospheric and Oceanic Technology* 2013; 30: 2233-2240. doi: 10.1175/JTECH-D-13-00077.1

2. Held DP, Mann J. Lidar Estimation of Rotor-Effective Wind Speed - An Experimental Comparison. *Wind Energy Science Discussions* 2019: 1-22. doi: 10.5194/wes-2018-72

3. Meng F, Lio WH, Larsen GC. Wind turbine LIDAR-assisted control: Power improvement, wind coherence and loads reduction. *Journal of Physics: Conference Series* 2022; 2265: 022060. doi: 10.1088/1742-6596/2265/2/022060

4. Lio WH, Meng F, Larsen GC. On LiDAR-assisted wind turbine retrofit control and fatigue load reductions. *Journal of Physics: Conference Series* 2022; 2265: 032072. doi: 10.1088/1742-6596/2265/3/032072

5. Meng F, Wenske J, Gambier A. Wind turbine loads reduction using feedforward feedback collective pitch control based on the estimated effective wind speed. *Proceedings of the American Control Conference* 2016; 2016-July: 2289-2294. doi: 10.1109/ACC.2016.7525259

6. Sinner M, Pao LY. Revisiting disturbance accommodating control for wind turbines. *Journal of Physics: Conference Series* 2020; 1618. doi: 10.1088/1742-6596/1618/2/022021

7. Aho J, Buckspan A, Pao L, Fleming P. An Active Power Control System for Wind Turbines Capable of Primary and Secondary Frequency Control for Supporting Grid Reliability. *AIAA/ASME Wind Symposium* 2013: 1-13. doi: 10.1.1.258.5692

8. Lio AWH, Meng F. Effective wind speed estimation for wind turbines in down-regulation. *Journal of Physics: Conference Series* 2020; 1452: 012008. doi: 10.1088/1742-6596/1452/1/012008

9. Hooft v. dE, Engelen vT. Estimated wind speed feed forward control for wind turbine operation optimisation. In: ; 2004: 22-25.

10. Østergaard KZ, Brath P, Stoustrup J. Estimation of effective wind speed. *Journal of Physics: Conference Series* 2007; 75: 012082. doi: 10.1088/1742-6596/75/1/012082

11. Henriksen L, Hansen M, Poulsen N. A simplified dynamic inflow model and its effect on the performance of free mean wind speed estimation. *Wind Energy* 2013; 16: 1213-1224. doi: 10.1002/we.1548

12. Bhowmik S, Spee R. Wind speed estimation based variable speed wind power generation. In: . 2. IEEE; 1998: 596-601

13. Ma X, Poulsen NK, Bindner H. Estimation of Wind Speed in Connection to a Wind Turbine. 1995.

14. Moustakis N, Mulders SP, Kober J, Wingerden vJ. A Practical Bayesian Optimization Approach for the Optimal Estimation of the Rotor Effective Wind Speed. *2019 American Control Conference (ACC)* 2019: 4179-4185.

15. Knudsen T, Bak T, Soltani M. Prediction models for wind speed at turbine locations in a wind farm. *Wind Energy* 2011; 14: 877-894. doi: 10.1002/we.491

16. Lio WH, Meng F. Kalman-based interacting multiple-model wind speed estimator for wind turbines. *IFAC PapersOnLine* 2020; 53: 12644-12649. doi: 10.1016/j.ifacol.2020.12.1840

17. Ortega R, Mancilla-David F, Jaramillo F. A globally convergent wind speed estimator for windmill systems. *Proceedings of the IEEE Conference on Decision and Control* 2011: 6079-6084. doi: 10.1109/CDC.2011.6160544

18. Ortega R, Mancilla-David F, Jaramillo F. A globally convergent wind speed estimator for wind turbine systems. *International Journal of Adaptive Control and Signal Processing* 2013; 27: 413-425. doi: 10.1002/acs.2319

19. Liu Y, Pamososuryo AK, Ferrari RM, Wingerden JWV. The Immersion and Invariance Wind Speed Estimator Revisited and New Results. *IEEE Control Systems Letters* 2022; 6: 361-366. doi: 10.1109/LCSYS.2021.3076040

20. Knudsen T, Bak T. Simple model for describing and estimating wind turbine dynamic inflow. *Proceedings of the American Control Conference* 2013: 640-646. doi: 10.1109/acc.2013.6579909

21. Simley E, Pao LY. Evaluation of a wind speed estimator for effective hub-height and shear components. In: . 19. John Wiley and Sons Ltd; 2016: 167-184

22. Soltani MN, Knudsen T, Svenstrup M, et al. Estimation of rotor effective wind speed: A comparison. *IEEE Transactions on Control Systems Technology* 2013; 21: 1155-1167. doi: 10.1109/TCST.2013.2260751

23. Dong L, Lio WH, Simley E. On turbulence models and lidar measurements for wind turbine control. *Wind Energy Science* 2021; 6: 1491-1500. doi: 10.5194/wes-6-1491-2021

24. Simley E, Pao L. Reducing LIDAR wind speed measurement error with optimal filtering. In: IEEE; 2013: 621-627

25. Schlipf D, Fleming P, Haizmann F, et al. Field Testing of Feedforward Collective Pitch Control on the CART2 Using a Nacelle-Based Lidar Scanner. In: ; 2012

26. Odgaard PF, Nielsen R, Damgaard C. On-line estimation of wind turbine power coefficients using unknown input observers. In: . 17. IFAC; 2008: 10646-10651

27. Lio WH, Li A, Meng F. Real-time rotor effective wind speed estimation using Gaussian process regression and Kalman filtering. *Renewable Energy* 2021; 169: 670-686. doi: 10.1016/j.renene.2021.01.040

28. Meng F, Lio AWH, Liew J. The effect of minimum thrust coefficient control strategy on power output and loads of a wind farm. *Journal of Physics: Conference Series* 2020; 1452. doi: 10.1088/1742-6596/1452/1/012009

29. Pedersen MM, Larsen GC. Integrated wind farm layout and control optimization. *Wind Energy Science* 2020; 5: 1551-1566. doi: 10.5194/wes-5-1551-2020

30. Frederik J, Weber R, Cacciola S, et al. Periodic dynamic induction control of wind farms : proving the potential in simulations and wind tunnel experiments. *Wind Energy Science* 2019: 1-18. doi: wes-2019-50

31. Burton T, Jenkins N, Sharpe D, Bossanyi E. *Wind Energy Handbook*. John Wiley Sons, Ltd . 2011

32. Selvam K, Kanev S, Wingerden vJW, Engelen vT, Verhaegen M. Feedback-feedforward individual pitch control for wind turbine load reduction. *International Journal of Robust and Nonlinear Control* 2009; 19: 72-91. doi: 10.1002/rnc.1324

33. Kalman RE. A New Approach to Linear Filtering and Prediction Problems. *Journal of Basic Engineering* 1960; 82: 35. doi: 10.1115/1.3662552

34. Brown RG, Hwang PY. *Introduction to Random Signals and Applied Kalman Filtering with Matlab Exercises*. Wiley. 4 ed. 2012.

35. Simley E, Pao LY. Evaluation of a wind speed estimator for effective hub-height and shear components. *Wind Energy* 2016; 19: 167-184. doi: 10.1002/we.1817

36. Pena A, J M, Thorsen GR. SpinnerLidar measurements for the CCA V52. *DTUWind Energy E-Report-0177* 2019.

37. Machefaux E, Larsen GC, Troldborg N, Gaunaa M, Rettenmeier A. Empirical modeling of single-wake advection and expansion using full-scale pulsed lidar-based measurements. *Wind Energy* 2015; 18: 2085-2103. doi: 10.1002/we.1805

38. Andersen SJ, Karikari-Boateng A, Bowie A, et al. TotalControl D3.9: Predictive Wind Field Model. *TotalControl* 2021.

39. Bar-Shalom Y, Li XR, Kirubarajan T. *Estimation with Applications to Tracking and Navigation*. John Wiley Sons, Inc. . 2001

40. Hansen MH, Henriksen LC, Tibaldi C, et al. HAWCStab2 User Manual. 2018.